

# Crossover in Hump-shape Hall Effect from Karplus-Luttinger to Topological Origins

## Elucidated by In-plane Magnetic Fields

Z. S. Lim<sup>1</sup>, A. K. H. Khoo<sup>2</sup>, L. E. Chow<sup>1</sup>, M. I. Sim<sup>3</sup>, H. J. Kirit<sup>1</sup>, G. J. Omar<sup>1</sup>, Z. Y. Luo<sup>1</sup>, P. Yang<sup>4</sup>, Z. T. Zhang<sup>1</sup>, H. Yan<sup>1</sup>, A. Soumyanarayanan<sup>3</sup>, R. Laskowski<sup>2</sup>, A. Ariando<sup>1</sup>

1. Physics Department, Block S12, #2 Science Drive 3, National University of Singapore 117551

2. Institute of High Performance Computing (IHPC), A\*STAR, Fusionopolis Way, #16-16 Connexis, Singapore 138632

3. Institute of Materials Research and Engineering (IMRE), A\*STAR, 2 Fusionopolis Way, Singapore 138634

4. Singapore Synchrotron Light Source (SSLS), 5 Research Link, Buona Vista, Singapore 117603

Email: [ariando@nus.edu.sg](mailto:ariando@nus.edu.sg)

### Abstract:

Among heterostructures involving oxides or topological insulator thin films, intensive debates circling the origins of hump-shape unconventional Hall Effects have emerged, with numerous magnetic imaging observations suggesting different interpretations. In general, confusion arose since the Hall-humps can be produced by either two overlapping loops of the Karplus-Luttinger mechanism corresponding to inhomogeneous collinear magnetic domains with perpendicular anisotropy, or the topological Hall Effect associated with Skyrmion-like magnetic textures with a net scalar spin chirality. In this work, using several heterostructures characterized by magnetic field rotation, we classified the crossover between the two origins of Hall-humps using a divergence exponent of peak field. For the former origin, the role of in-plane field is understood to be spin-orbit torque driving domain expansion, while for the latter it is the destruction of  $3\mathbf{q}$  spin-wave superposition of Skyrmion-lattice from Ginzburg-Landau theory. We also obtained a linear scaling of the divergence exponent with domain wall energy among various material systems.

## Article:

Theoretical development on Anomalous Hall Effect (AHE) began in 1954 when Karplus and Luttinger (KL)<sup>1</sup> pioneered the formulation of perpendicular electron velocity of the intrinsic mechanism in simple ferromagnetic metals,  $v_{\perp} = \frac{1}{i\hbar} [\hat{H}_{\text{SOC}}, x_{\perp}] = \frac{1}{m^2 c^2} \left( \frac{\mathbf{M}}{M_s} \times \nabla V \right)$ , where spin-orbit coupling (SOC) is the crucial perturbation to the system subjected to an external electric field  $\nabla V$ . It was later refined by McDonald and Nagaosa et al. using the language of k-space Berry curvature  $\mathbf{\Omega}(\mathbf{k})$  to account for band structure details<sup>2, 3</sup>. Whereas the skew scattering and side-jump extrinsic mechanisms involving impurity scattering were formulated by Smit using Fermi Golden Rule<sup>4</sup>, and by Berger<sup>5</sup>, Norzières and Lewiner<sup>6</sup> respectively. These three sideways deflection mechanisms, all of which require SOC on a uniform collinear magnetization ( $M$ ) background, formed the backbone of AHE<sup>7</sup> analyses via  $\rho_{xy}^A(H) \propto \rho_{xx}^{\beta} M(H)$  with  $1 \leq \beta \leq 2$  as the experimentally-extracted exponents, until the last two decades. Then, the pronounced enhancement of non-linear  $\rho_{xy}(H, T)$  near Curie temperature ( $T_C$ ) observed in perovskite manganites<sup>8, 9</sup> did not agree with the mentioned conventional AHE mechanisms. This motivated extensive theoretical study into the unconventional *subset* of AHE from fluctuating chiral arrangements of magnetic moments in the real-space with net scalar spin chirality  $\chi_{\text{SSC}} = \sum_{ijk} (\mathbf{m}_i \times \mathbf{m}_j) \cdot \mathbf{m}_k$ . In contrast, such *Topological Hall Effect* (THE) does not require SOC<sup>10, 11</sup>, although the underlying texture formation may involve SOC-induced Dzyaloshinskii-Moriya Interaction (DMI) or crystallographic frustration. In the typical regime where the Skyrmions' radii are large compared to electrons' mean free path i.e.  $r_{sk} \gg l_{mf}$ , solving the Schrodinger equation with a strong and adiabatic Hund's coupling between the electrons' spin ( $s$ ) and local moment ( $\mathbf{m}$ ) requires a unitary transformation of reference frame for neighbouring moments<sup>12</sup>. Hence, an additional vector potential arises in the canonical momentum, yielding a real-space pseudo-

magnetic field  $B_{\text{eff}} = \frac{1}{4\pi} \int \mathbf{m} \cdot \left( \frac{\partial \mathbf{m}}{\partial x} \times \frac{\partial \mathbf{m}}{\partial y} \right) dx dy$  to be included into  $\rho_{xy}^T(H) \propto \frac{B_{\text{eff}}}{ne}$ , in analogy to the ordinary Hall Effect (OHE)<sup>13</sup>. However, in the opposite regime of  $r_{sk} \approx a \ll l_{mf}$  where  $a$  is the lattice parameter, THE can also be calculated from Kubo formula in k-space, and tight-binding models often produced a massive Dirac Fermion band structure<sup>14</sup>.

In electrical transport experiments, the differences between the two mentioned AHE *subsets* (i.e. the KL mechanism for collinear ferromagnets and THE for chiral textures) can be subtle. They are easily distinguishable if: the former  $\rho_{xy}^{KL}(H_z) \propto M(H_z)$  follows the simple Langevin shape like  $\mathcal{L}(H_z) \sim \coth(H_z) - 1/H_z$ ; while the latter  $\rho_{xy}^T(H_z)$  follows the typical field-evolution of Skyrmion density, i.e.: nucleation  $\rightarrow$  maximum  $\rightarrow$  saturation with increasing  $H_z$ , hence forming anti-symmetric humps of shape  $\sim \mathcal{L}(H_z)/H_z$ . Such Hall-humps have been observed in many heterostructures of oxide<sup>15, 16, 17</sup> or topological insulator (TI)<sup>18, 19, 20, 21</sup> thin films. However, ambiguity arose when numerous recent publications saw the possibility of overlapping two KL-AHE loops to fit the experimentally observed Hall-humps, implying that the material systems in question contain inhomogeneous collinear (trivial) domains, and doubting the existence of real-space topological Skyrmions. Hence, intensive efforts were invested on magnetic imaging to resolve the ambiguity in those low-temperature and low-magnetization materials using magnetic force microscopy (MFM)<sup>22, 23</sup>, X-ray Photoemission Microscopy (XMCD-PEEM)<sup>24, 25</sup>. However, less emphasis was placed on measuring the domain wall energy ( $\sigma_{DW}$ ), nor the topological numbers (topological charge (Q), vorticity ( $Q_v$ ), helicity ( $Q_h$ ))<sup>26, 27</sup> if Skyrmions were claimed. Lorentz Transmission Electron Microscopy is often inapplicable for thin films due to low magnetic interaction volume. Notably, a single-layer ultrathin SrRuO<sub>3</sub> (SRO) with terrace engineering was shown to produced trivial domains segregation<sup>28</sup> corresponding to the Hall-humps in favour fully of the trivial interpretation; yet SrRuO<sub>3</sub>/PbTiO<sub>3</sub> obtained a square lattice from 2q-spin-waves

perpendicular superposition<sup>29</sup> akin to an intermediate regime. In this work, we present a novel analysis scheme on Hall-humps peak fields ( $H_{\text{peak}}$ ) evolving under magnetic field rotation in several heterostructures with comprehensive magnetic properties. We provide convincing explanations for the trivial cases using spin-orbit torque (SOT) induced domain expansion, and for the topological cases using micromagnetic simulation. We also postulate that a trend of  $H_{\text{peak}}$  shift with varying  $\sigma_{\text{DW}}$  exists among various material systems constituting a continuous spectrum between the two extreme regimes of trivial domain and topological Skyrmions. Such analysis may potentially become a useful protocol for future disambiguation.

Figure 1 presents the selected four heterostructures for analyses, with sample fabrication details described in *methods*. Perovskite SRO films are well-known to have two distinct structural phases, i.e.: the monoclinic (m-) and tetragonal (t-) phases stabilized at 100 mTorr and 10 mTorr respectively in a typical Pulsed Laser Deposition (PLD) setup. Their glazer notations of octahedral rotations/tilts are distinguished as  $a^-b^+c^-$  and  $a^0a^0c^0$  respectively from half-integer X-ray Bragg diffraction<sup>30</sup> (in Figure S1). Their square KL-AHE loops also differ significantly – negative sign for m-SRO and positive for t-SRO without temperature sign change. This difference in the two phases can be understood from the opposite signs of k-space Berry curvature in different 4d  $t_{2g}$  bands, since t-SRO is known to have lower moment of  $\sim 1.0 \mu_{\text{B}}/\text{f.u.}$  compared to  $\sim 1.6 \mu_{\text{B}}/\text{f.u.}$  in m-SRO<sup>16, 28</sup>. In Figure 1b, the “mR<sub>3</sub>tR<sub>7</sub>” structure formed by ultrathin m-SRO(3uc) on t-SRO(7uc) grown on SrTiO<sub>3</sub>(001) produced obvious Hall-humps ranging from 3 K to 40 K. The mR<sub>3</sub>tR<sub>7</sub> was deliberately engineered to exhibit z-direction phase separation, which can represent many recent publications around single-layer SRO including those with xy-plane inhomogeneity<sup>16, 28, 31, 32</sup>. This is generally valid since an ultrathin t-phase buffer layer is often inevitable when SRO is interfaced directly with the cubic SrTiO<sub>3</sub>(001) surface due to suppression of octahedral rotations/tilts<sup>33</sup>, regardless of the intended growth pressure or substrate’s surface termination. Meanwhile, the



“mR<sub>5</sub>I<sub>10</sub>” structure in Figure 1c constructed by m-SRO(5uc) on SrIrO<sub>3</sub>(10uc) also showed large Hall-humps across a wide temperature range of 10-90 K. Here the paramagnetic SrIrO<sub>3</sub> is believed to contribute strong SOC and DMI, as well as a buffer layer with thickness beyond the octahedral suppression region so that the m-SRO layer above can be proven to be free from phase separation issue. This has been discussed in reference [34] where a DMI of 0.76 mJ/m<sup>2</sup> was obtained from *ab-initio* calculations by taking account of the mismatch in octahedral tilt at the SRO(*a<sup>-</sup>b<sup>+</sup>c<sup>0</sup>*)/SIO(*a<sup>+</sup>b<sup>0</sup>c<sup>0</sup>*) interface. The half-integer X-ray Diffractions, structural models and ab-initio calculations were repeated for mR<sub>3</sub>tR<sub>7</sub> in this work and are presented in Supplementary Figure S1 and S2.

To shed light on the universality of our subsequent analyses, we also included the 8uc and 3uc Tm<sub>3</sub>Fe<sub>5</sub>O<sub>12</sub>(TmIG) films capped with Pt(2nm) on Gd<sub>3</sub>Ga<sub>5</sub>O<sub>12</sub>(1111) substrates, labelled as “P<sub>2</sub>T<sub>8</sub>” and “P<sub>2</sub>T<sub>3</sub>”, as shown in Figure 1d. Here, TmIG(111) is renowned to be a high-*T<sub>C</sub>* ferrimagnetic insulator with perpendicular anisotropy (PMA) under tensile strain, hence the spin current reflected off the Pt/TmIG interface can detect clear Spin Hall Effect (SHE) induced square KL-AHE loop in P<sub>2</sub>T<sub>8</sub><sup>35, 36, 37</sup> and THE in P<sub>2</sub>T<sub>3</sub><sup>38, 39, 40</sup> at 300 K. Unlike the hysteretic Hall-humps in mR<sub>3</sub>tR<sub>7</sub> and mR<sub>5</sub>I<sub>10</sub> well below their respective *T<sub>C</sub>* of 150 K and 100 K, the magnitude of the non-hysteretic Hall-humps in P<sub>2</sub>T<sub>3</sub> is greatly enhanced around *T<sub>C</sub>*~300 K of the ultrathin (3uc) TmIG, but vanishes at low temperatures. Such phenomenon has been discussed as the chiral fluctuation behaviour<sup>17</sup> with a proximity-magnetized Pt in its carrier localization regime, and exhibits a power-law enhancement around the 2<sup>nd</sup>-order transition temperature<sup>41</sup>.

### **Total field rotation scheme**

The main focus of this work is the investigation of Hall effects with rotation of magnetic field direction ( $\rho_{xy}(\theta, H)$ ) from out-of-plane ( $\mathbf{H} \parallel \mathbf{z}$  at  $\theta=0^\circ$ ) approaching in-plane

( $\mathbf{H} \parallel \mathbf{x}$  at  $\theta \rightarrow 90^\circ$ ), done at 20 K for mR<sub>3</sub>tR<sub>7</sub> and mR<sub>5</sub>I<sub>10</sub> and 300 K for P<sub>2</sub>T<sub>8</sub> and P<sub>2</sub>T<sub>3</sub>. The measurement scheme is illustrated in Figure 2 (top panel), presented in total field,  $H_{\text{total}} = \sqrt{H_z^2 + H_x^2}$ , implying the field sweep is in the 1<sup>st</sup> and 3<sup>rd</sup> quadrants. Notably in Figure 2a,  $H_{\text{peak}}$  of mR<sub>3</sub>tR<sub>7</sub> exhibited fast divergence with increasing  $\theta$  (left panel), and the trend can be fitted with a phenomenological  $H_{\text{peak}} \propto 1/\cos^\gamma(\theta)$  to obtain the exponent  $\gamma=0.74$  (right panel). Note that the  $\gamma=1$  limit implies zero contribution from the in-plane field. It is instructive to decompose the Hall data of mR<sub>3</sub>tR<sub>7</sub> at  $\theta=0^\circ$  into two opposite-sign KL-AHE loops via  $\rho_{xy}(H, \theta) = \sum_{i=1,2} A_i \left\{ \coth \left[ B_i \left( H - \frac{H_{c,i}(\theta=0)}{\cos^\gamma(\theta)} \right) \right] - \left[ B_i \left( H - \frac{H_{c,i}(\theta=0)}{\cos^\gamma(\theta)} \right) \right]^{-1} \right\}$  where  $A_i$  and  $B_i$  are coefficients, and Hall-humps will emerge at field range between the two coercive fields ( $H_{C1,2}$ ). By incorporating  $\gamma=0.74$ , experimental data at larger  $\theta$ -angles can be well-reproduced. Such  $\theta$ -dependent Hall analysis, albeit unprecedented, supports that mR<sub>3</sub>tR<sub>7</sub> hosts trivial inhomogeneous domains with opposite-sign KL-AHEs at intermediate fields in agreement to reference<sup>28</sup>, unrelated to Skyrmions. Likewise, the KL-AHE of P<sub>2</sub>T<sub>8</sub> in Figure 2c also showed clear divergence of  $H_C \propto 1/\cos^{0.45}(\theta)$ . However, the  $H_{\text{peak}}$  of mR<sub>5</sub>I<sub>10</sub> and P<sub>2</sub>T<sub>3</sub> were found to be independent of  $\theta$  with  $\gamma \sim 0.06$  and  $0.04$  respectively while the hump magnitudes ( $\Delta\rho_{xy}$ ) also diminished at large  $\theta$ -angles, as shown in Figures 2b,d. These observations suggest grouping mR<sub>3</sub>tR<sub>7</sub> and P<sub>2</sub>T<sub>8</sub> together with the behaviour of trivial domain, while mR<sub>5</sub>I<sub>10</sub> and P<sub>2</sub>T<sub>3</sub> are in the group of topological Skyrmions hosts.

### Resolved field components scheme

To understand the significant divergence reflected by  $\gamma=0.74$  and  $0.45$  in mR<sub>3</sub>tR<sub>7</sub> and P<sub>2</sub>T<sub>8</sub> respectively, we further resolved the out-of-plane ( $H_z$ ) and in-plane ( $H_x$ ) field components by a suitably engineered Labview program, as described in *methods*. Hence, Hall measurements can be done with sweeping  $H_z$  with constant nonzero  $H_x$ , while the total field vector is rotating in the 1<sup>st</sup> and 2<sup>nd</sup> quadrants or the 4<sup>th</sup> and 3<sup>rd</sup> quadrants for a particular

$\rho_{xy}(H_z, H_x)$  loop (schematic shown in Figure 3 top). In Figure 3a, clear shifting of z-component peak field  $H_{\text{peak},z}$  towards left and right sides were observed in mR3tR7 when  $\mu_0 H_x$  were varied in the range of  $\pm 3$  T. Notably, the loop width demarcated by the  $\pm H_{\text{peak},z}$  stayed almost constant, thus the  $\mp H_{\text{peak},z}$  opposite to the shift direction can surprisingly reach 0 at large  $\pm H_x$ . Likewise in Figure 3b, the z-component coercive field ( $H_{C,z}$ ) in KL-AHE of P2T8 also shifted towards left and right sides akin to an exchange bias, together with loop width shrinkage on top of the shift.

Here we point out that the shifts  $\rho_{xy}(H_z)$  loops observed in both mR3tR7 and P2T8 with varying  $H_x$  is a clear signature of in-plane field assisted SOT on trivial collinear domains, which has been popular in reducing the switching current density in SOT experiments<sup>42</sup> as well as DMI measurements<sup>43</sup>. This is illustrated in Figure 3c by a bubble domain with collinear magnetizations at the centre and surrounding bordered by an arbitrarily-shaped domain wall, which adequately represents those stabilized by dipolar interactions. Here, a spin current ( $\mathbf{J}_{s,z}$ ) carrying a spin-angular ( $\mathbf{s}_y$ ) is injected by a low charge current ( $\mathbf{J}_{c,x}$ ) due to SHE, and is effectively absorbed by Néel-type domain walls aligning along x-direction ( $\pm \mathbf{m}_{\text{DW},x}$ ). This produces SOT effective field  $\mathbf{H}_{\text{SOT},z} \propto \mathbf{s}_y \times \mathbf{m}_{\text{DW}}$  that exerts a damping-like torque,  $\frac{d\mathbf{m}_{\text{DW}}}{dt} = -\alpha_G \mathbf{m}_{\text{DW}} \times \mathbf{m}_{\text{DW}} \times \mathbf{H}_{\text{SOT},z}$  onto the domain walls, where  $\alpha_G$  is the Gilbert damping. At absence of in-plane field ( $H_x=0$ ), the  $\mathbf{H}_{\text{SOT},z}$  at opposite sides of the domain are antiparallel (top panel), which causes parallel domain wall velocities ( $v_{\text{DW}}$ ) along x-direction and hence domain movement only (top panel). However, with the presence of  $H_x$  aligning most  $\mathbf{m}_{\text{DW},x}$  (bottom panel), the domain walls move in opposite directions resulting domain expansion/shrinkage<sup>44</sup>. This way, the bi-stability of  $\pm M_z$  domains with respect to  $H_z$  is biased, i.e.: it is easier to switch down but harder to switch up for  $+H_x$  and is manifested as a right-shift of  $\rho_{xy}(H_z)$  loops, and vice-versa for  $-H_x$ . Besides, P2T8 also exhibited an additional

loop-narrowing effect ( $\pm H_{c,z}$  reduction) at the small  $\pm H_x$  regimes which is absent in mR<sub>3</sub>tR<sub>7</sub>. This effect can be understood from purely magnetic field torque acting on  $\pm M_z$  domains causing easier switching by  $H_z$  regardless of polarity and is irrelevant to SOT on  $m_{DW}$ . Since the  $H_z$  loop-narrowing effect is absent in mR<sub>3</sub>tR<sub>7</sub>, trivial magnetic bubbles can be inferred to be dominant in mR<sub>3</sub>tR<sub>7</sub> with abundant DWs, while P<sub>2</sub>T<sub>8</sub> is closer to abrupt single collinear  $M_z$  domain switching. In an overview, for mR<sub>3</sub>tR<sub>7</sub> and P<sub>2</sub>T<sub>8</sub>, we note that the observed  $H_T$ -loop expansion trend in the total field rotation scheme (Figure 2) is consistent to the observed  $H_z$ -loop shifting trend in the resolved field components scheme (Figure 3), since the former which involves field sweep in the 1<sup>st</sup>-3<sup>rd</sup> (or 4<sup>th</sup>-2<sup>nd</sup>) quadrants causes increasing switching difficulty to both polarity of  $\pm M_z$ . The inter-conversion of data in these two schemes is illustrated in supplementary Figure S3a,b. To support the relevance of the damping-like SOT on domain walls, the  $\rho_{xy}(H_z)$  loop shift with varying  $J_{c,x}$  is also evident in P<sub>2</sub>T<sub>8</sub> (supplementary Figure S3c,d), showing a reversal of shift trend with opposite  $H_x$  polarities consistent to past publications. Our investigation was limited to small current densities regime so that Joule heating effect is mitigated.

Conversely, in Figures 4a,b, mR<sub>5</sub>I<sub>10</sub> and P<sub>2</sub>T<sub>3</sub> showed stationary  $H_{z,peak}$  without left/right shifting but fast-vanishing Hall-humps with varying  $H_x$  under the same field components resolving scheme. Combining evidences from Figures 2b,d and 4a,b, it is convincing to rule out the existence of trivial domain inhomogeneity in mR<sub>5</sub>I<sub>10</sub> and P<sub>2</sub>T<sub>3</sub> heterostructures. To double-check with Skyrmions properties, we performed MUMAX<sup>3</sup> micromagnetic simulations<sup>45</sup> of Néel-type magnetic Skyrmions by using realistic parameters extracted from magnetometry (Supplementary Figure S4a,b). Here the saturation magnetization ( $M_{sat}$ ) in mR<sub>5</sub>I<sub>10</sub> and the interfacial DMI ( $D_{ind}$ ) in P<sub>2</sub>T<sub>3</sub> were carefully optimized as free parameters within reasonable range, so that the simulated peaks of topological charge density ( $TCD$ ) =  $\frac{1}{4\pi} \hat{\mathbf{m}} \cdot \left( \frac{\partial \hat{\mathbf{m}}}{\partial x} \times \frac{\partial \hat{\mathbf{m}}}{\partial y} \right)$  can be matched exactly to the

respective  $H_{\text{peak}}$  of Hall-humps at  $\theta=0^\circ$  ( $=1.0$  T and  $0.1$  T), with details written in the Supplementary text. Consistent to the respective Hall-humps, the field-dependent  $TCD(H)$  peaks for mR5I10 are hysteretic but is non-hysteretic for P2T3. In Figures 4c,d, the  $TCD(\theta, H)$  mappings obtained for both the structures show that the total fields corresponding to the densest Skyrmion-lattice (SkL) remain constant with increasing  $\theta$ . This can be explained by the Landau-Ginzburg framework for triple- $\mathbf{q}$  spin-waves superposition. It is well-known that a trio of cycloidal spin-waves that can be described by  $\mathbf{m}_i = \sum_i^{1,2,3} [\mathbf{m}_z \cos(\mathbf{q}_i \cdot \hat{\mathbf{r}}) \pm \sin(\mathbf{q}_i \cdot \hat{\mathbf{r}})]$  would create a two-dimensional (2D) hexagonal-close-packed Néel-SkL stabilized by a small  $H_z$ , where  $\hat{\mathbf{r}} = [\hat{x}, \hat{y}, \hat{z}]$ ,  $\mathbf{m}_z = [0, 0, 1]$ , and wave vectors  $\mathbf{q}_i = [\cos(\frac{2\pi i}{3}), \sin(\frac{2\pi i}{3}), 0]$ . Likewise, helicoidal spin-waves with  $\mathbf{m}_i = \sum_i^{1,2,3} [\mathbf{m}_z \cos(\mathbf{k}_i \cdot \hat{\mathbf{r}}) \pm (\mathbf{m}_z \times \mathbf{q}_i) \sin(\mathbf{k}_i \cdot \hat{\mathbf{r}})]$  would create a 2D Bloch-type SkL. Then, application of  $H_x$  would cause  $\mathbf{m}$  to precess around  $H_x$ , hence the dominant single- $\mathbf{q}$  is perpendicular and parallel to  $H_x$  for the Néel- and Bloch-type cases<sup>46, 47</sup>. Due to this vulnerability of SkLs subjected to in-plane fields, the total field of peak  $TCD$  will not diverge but is rather independent of  $\theta$ -angle ( $\gamma \sim 0$ ).

### Summary of trend

Lastly, theoretical understanding has established that the crucial difference between trivial domains and topological textures lies at the domain wall energy  $\sigma_{\text{DW}} = 4\sqrt{A_{\text{ex}}K_{\text{U}}} - \pi D$ , which is positive for trivial and negative for topological<sup>48</sup>, where  $A_{\text{ex}}$ ,  $K_{\text{U}}$  and  $D$  are the exchange stiffness, uniaxial anisotropy and interfacial DMI respectively. Hence, it would be insightful to repeat the total field rotation scheme for a plethora of other heterostructures, assuming that  $\gamma$  is a good quantification parameter for Hall-hump shift due to in-plane magnetic field or the likelihood of trivial domains. As shown in Figure 5, a linear relationship between the scaling exponent  $\gamma$  and  $\sigma_{\text{DW}}$  was found. In particular, the SrRuO<sub>3</sub>/BaTiO<sub>3</sub> bilayer

and superlattice heterostructures can be found at the intermediate regime of the plot, while their magnetometry and  $\gamma$  extractions data are presented in supplementary Figure S4c-f. Such systems might be potentially ambiguous since the interfacial DMI was calculated by first-principle to be quite large ( $\sim 0.84$  mJ/m<sup>2</sup>)<sup>49</sup>, yet a consensus about the magnetic texture identity corresponding to the Hall-humps has not been reached in imaging<sup>29</sup>. Here, the observed  $\gamma \sim 0.3-0.5$  may likely be an inspiring bridge to understand that the SrRuO<sub>3</sub>/BaTiO<sub>3</sub> heterostructures are in the mixed trivial bubbles and Skyrmions regime, since its tetragonal crystal structure contributes a large  $K_U$ . A mixed state could have similar topology to genuine Skyrmions but enjoy less topological protection. Without the in-plane field schemes to scrutinize textures movement, expansion or annihilation, a general imaging technique would still be difficult to reach a sound conclusion for such mixed state. One may also envision a reducing trend of threshold current density of moving the Skyrmions or bubble domains by SOT with reducing  $\gamma$ , consistent to the idea of topological protection and evasion of impurity pinning<sup>50</sup>, but is currently out-of-scope in this work.

In conclusions, the gradual crossover of Hall-humps with origin from KL-AHE to THE has been elucidated by observing the response of Hall-humps to in-plane magnetic fields to correspond with the fundamental understanding of how trivial domains and genuine magnetic Skyrmions should behave. This method may potentially become a useful protocol in complementing future Skyrmion imaging efforts and development of topological spintronics.

**Methods:**

For structures mR<sub>3</sub>tR<sub>7</sub> and mR<sub>5</sub>I<sub>10</sub>, the STO(001) substrates' surface were etched by buffered-HF solutions and annealed at 950°C for 1.5 hours to achieve single TiO<sub>2</sub>-termination. Hall-bars were defined by insulating amorphous AlN film with thickness ~200 nm on the STO(001) substrates by photolithography and lift-off. Next, crystalline SRO and SIO films were grown on the exposed STO surface at 600°C and 700°C temperatures respectively and oxygen pressure PO<sub>2</sub>=100 mTorr. The B<sub>12</sub>S<sub>8</sub> was constructed by 8.5uc of SRO film grown on STO(001) at 600°C and PO<sub>2</sub>=100 mTorr, followed by 12uc BTO at PO<sub>2</sub>=2 mTorr and same temperature. The extra 0.5uc of SRO is to account for termination change from TiO<sub>2</sub> to SrO at the 1<sup>st</sup> uc. Whereas the (B<sub>4</sub>S<sub>4</sub>)<sub>x4</sub>-SL is actually a superlattice of [SRO(4uc) on BTO(4uc)]<sub>x4</sub> capped with a final 4uc BTO, constructed by alternating BTO at PO<sub>2</sub>=10 mTorr and SRO at PO<sub>2</sub>=50 mTorr at a common temperature 650°C. The materials deposited on AlN are amorphous and insulating. For structures P<sub>2</sub>T<sub>8</sub> and P<sub>2</sub>T<sub>3</sub>, the GGG(111) substrates which were annealed at 1000°C and 6 hours. Then, crystalline TmIG films were grown directly on the substrates at 700°C and PO<sub>2</sub>=15 mTorr, before *in-situ* transfer to a sputtering chamber for amorphous Pt capping at room temperature. Finally, Hall-bars were defined by photolithography and ion beam milling. All films have minimal surface roughness of ~rms. 0.2 nm without island growth (step-flow and layer-by-layer for SRO and SIO respectively), so that high quality interfaces are ensured. Electrical measurements were done in a Quantum Design Physical Properties Measurement System (PPMS-6000) equipped with a rotator attachment, while and magnetometry was measured in a Superconducting Quantum Interference Device (SQUID). X-ray diffraction was measured in the Singapore Synchrotron Light Source (SSLS).

**Conflict of Interest:**

The authors declare no financial interest.

**Author contributions:**

Z. S. Lim prepared the samples, did electrical measurement, conceived the full research idea and prepared the manuscript. A. H. K. Khoo performed the DFT calculations. L. E. Chow proposed and prepared the  $mR_3tR_7$  structure. M. I. Sim measured the magnetometry. The other group members contributed valuable suggestions and improvements to the manuscript.

**Acknowledgement:**

This research is supported by the Agency for Science, Technology and Research (A\*STAR) under its Advanced Manufacturing and Engineering (AME) Individual Research Grant (IRG) (A1983c0034), the National University of Singapore (NUS) Academic Research Fund (A-0004196-00-00), and the Singapore National Research Foundation (NRF) under the Competitive Research Programs (CRP Award No. NRF-CRP15-2015-01).



## References:

1. Karplus R, Luttinger JM. Hall Effect in Ferromagnetics. *Phys. Rev.* **95**, 1154-1160 (1954).
2. Jungwirth T, Niu Q, MacDonald AH. Anomalous Hall Effect in Ferromagnetic Semiconductors. *Phys. Rev. Lett.* **88**, 207208 (2002).
3. Onoda M, Nagaosa N. Topological Nature of Anomalous Hall Effect in Ferromagnets. *J. Phys. Soc. Jpn.* **71**, 19-22 (2002).
4. Smit J. The spontaneous hall effect in ferromagnetics II. *Phy* **24**, 39-51 (1958).
5. Berger L. Side-Jump Mechanism for the Hall Effect of Ferromagnets. *Phys. Rev. B* **2**, 4559-4566 (1970).
6. Nozières P, Lewiner C. A simple theory of the anomalous hall effect in semiconductors. *J. Phys. (Paris)* **34**, 901-915 (1973).
7. Nagaosa N, Sinova J, Onoda S, MacDonald AH, Ong NP. Anomalous Hall effect. *Rev. Mod. Phys.* **82**, 1539-1592 (2010).
8. Chun SH, Salamon MB, Lyanda-Geller Y, Goldbart PM, Han PD. Magnetotransport in Manganites and the Role of Quantal Phases: Theory and Experiment. *Phys. Rev. Lett.* **84**, 757-760 (2000).
9. Ye J, Kim YB, Millis AJ, Shraiman BI, Majumdar P, Tešanović Z. Berry Phase Theory of the Anomalous Hall Effect: Application to Colossal Magnetoresistance Manganites. *Phys. Rev. Lett.* **83**, 3737-3740 (1999).
10. Zhang Y, *et al.* Strong anisotropic anomalous Hall effect and spin Hall effect in the chiral antiferromagnetic compounds  $Mn_3X$ , ( $X=Ge, Sn, Ga, Ir, Rh$ , and  $Pt$ ). *Phys. Rev. B* **95**, 075128 (2017).
11. Ishizuka H, Nagaosa N. Spin chirality induced skew scattering and anomalous Hall effect in chiral magnets. *Sci. Adv.* **4**, eaap9962 (2018).
12. Everschor-Sitte K, Sitte M. Real-space Berry phases: Skyrmion soccer (invited). *J. Appl. Phys.* **115**, 172602 (2014).
13. Bruno P, Dugaev VK, Taillefumier M. Topological Hall Effect and Berry Phase in Magnetic Nanostructures. *Phys. Rev. Lett.* **93**, 096806 (2004).
14. Hamamoto K, Ezawa M, Nagaosa N. Quantized topological Hall effect in skyrmion crystal. *Phys. Rev. B* **92**, 115417 (2015).
15. Matsuno J, *et al.* Interface-driven topological Hall effect in  $SrRuO_3$ - $SrIrO_3$  bilayer. *Sci. Adv.* **2**, e1600304 (2016).
16. Groenendijk DJ, *et al.* Berry phase engineering at oxide interfaces. *Phys. Rev. Res.* **2**, 023404 (2020).
17. Wang W, *et al.* Spin chirality fluctuation in two-dimensional ferromagnets with perpendicular magnetic anisotropy. *Nat. Mater.* **18**, 1054-1059 (2019).
18. Yasuda K, *et al.* Geometric Hall effects in topological insulator heterostructures. *Nat. Phys.* **12**, 555-559 (2016).
19. Liu C, *et al.* Dimensional Crossover-Induced Topological Hall Effect in a Magnetic Topological Insulator. *Phys. Rev. Lett.* **119**, 176809 (2017).
20. Fijalkowski KM, *et al.* Coexistence of Surface and Bulk Ferromagnetism Mimics Skyrmion Hall Effect in a Topological Insulator. *Phys. Rev. X* **10**, 011012 (2020).
21. Jiang J, *et al.* Concurrence of quantum anomalous Hall and topological Hall effects in magnetic topological insulator sandwich heterostructures. *Nat. Mater.*, (2020).
22. Vistoli L, *et al.* Giant topological Hall effect in correlated oxide thin films. *Nat. Phys.* **15**, 67-72 (2019).
23. Meng K-Y, *et al.* Observation of Nanoscale Skyrmions in  $SrIrO_3$ / $SrRuO_3$  Bilayers. *Nano Lett.* **19**, 3169-3175 (2019).

24. Skoropata E, *et al.* Interfacial tuning of chiral magnetic interactions for large topological Hall effects in LaMnO<sub>3</sub>/SrIrO<sub>3</sub> heterostructures. *Sci. Adv.* **6**, eaaz3902 (2020).
25. Zhang S, Kronast F, van der Laan G, Hesjedal T. Real-Space Observation of Skyrmionium in a Ferromagnet-Magnetic Topological Insulator Heterostructure. *Nano Lett.* **18**, 1057-1063 (2018).
26. Nagaosa N, Tokura Y. Topological properties and dynamics of magnetic skyrmions. *Nat. Nanotechnol.* **8**, 899 (2013).
27. Zhang X, *et al.* Skyrmion-electronics: writing, deleting, reading and processing magnetic skyrmions toward spintronic applications. *J. Phys.: Condens. Matter* **32**, 143001 (2020).
28. Wang L, Feng Q, Lee HG, Ko EK, Lu Q, Noh TW. Controllable Thickness Inhomogeneity and Berry Curvature Engineering of Anomalous Hall Effect in SrRuO<sub>3</sub> Ultrathin Films. *Nano Lett.* **20**, 2468-2477 (2020).
29. Seddon SD, *et al.* Real-space observation of ferroelectrically induced magnetic spin crystal in SrRuO<sub>3</sub>. *Nat. Commun.* **12**, 2007 (2021).
30. Lu W, Yang P, Song WD, Chow GM, Chen JS. Control of oxygen octahedral rotations and physical properties in SrRuO<sub>3</sub> films. *Phys. Rev. B* **88**, 214115 (2013).
31. Qin Q, *et al.* Emergence of Topological Hall Effect in a SrRuO<sub>3</sub> Single Layer. *Adv. Mater.* **31**, 1807008 (2019).
32. Kan D, Moriyama T, Kobayashi K, Shimakawa Y. Alternative to the topological interpretation of the transverse resistivity anomalies in SrRuO<sub>3</sub>. *Phys. Rev. B* **98**, 180408 (2018).
33. Liao Z, *et al.* Controlled lateral anisotropy in correlated manganite heterostructures by interface-engineered oxygen octahedral coupling. *Nat. Mater.* **15**, 425-431 (2016).
34. Zhi Shih Lim AKHK, Zhou Zhou, Ganesh Ji Omar, Ping Yang, Robert Laskowski, Ariando Ariando. Oxygen Octahedral Tilt Controlled Topological Hall Effect in Epitaxial and Freestanding SrRuO<sub>3</sub>/SrIrO<sub>3</sub> Heterostructures. *arXiv.org*, (2022).
35. Avci CO, *et al.* Current-induced switching in a magnetic insulator. *Nat. Mater.* **16**, 309-314 (2017).
36. Avci CO, *et al.* Interface-driven chiral magnetism and current-driven domain walls in insulating magnetic garnets. *Nat. Nanotechnol.* **14**, 561-566 (2019).
37. Vélez S, *et al.* High-speed domain wall racetracks in a magnetic insulator. *Nat. Commun.* **10**, 4750 (2019).
38. Ahmed AS, *et al.* Spin-Hall Topological Hall Effect in Highly Tunable Pt/Ferrimagnetic-Insulator Bilayers. *Nano Lett.* **19**, 5683-5688 (2019).
39. Shao Q, *et al.* Topological Hall effect at above room temperature in heterostructures composed of a magnetic insulator and a heavy metal. *Nat. Electron.* **2**, 182-186 (2019).
40. Lee AJ, *et al.* Probing the Source of the Interfacial Dzyaloshinskii-Moriya Interaction Responsible for the Topological Hall Effect in Metal/Tm<sub>3</sub>Fe<sub>5</sub>O<sub>12</sub> bilayers. *Phys. Rev. Lett.* **124**, 107201 (2020).
41. Raju M, *et al.* Colossal topological Hall effect at the transition between isolated and lattice-phase interfacial skyrmions. *Nat. Commun.* **12**, 2758 (2021).
42. Manchon A, *et al.* Current-induced spin-orbit torques in ferromagnetic and antiferromagnetic systems. *Rev. Mod. Phys.* **91**, 035004 (2019).
43. Caretta L, *et al.* Interfacial Dzyaloshinskii-Moriya interaction arising from rare-earth orbital magnetism in insulating magnetic oxides. *Nat. Commun.* **11**, 1090 (2020).

44. Pai C-F, Mann M, Tan AJ, Beach GSD. Determination of spin torque efficiencies in heterostructures with perpendicular magnetic anisotropy. *Phys. Rev. B* **93**, 144409 (2016).
45. Vansteenkiste A, Leliaert J, Dvornik M, Helsen M, Garcia-Sanchez F, Waeyenberge BV. The design and verification of MuMax3. *AIP Advances* **4**, 107133 (2014).
46. Leonov AO, Kézsmárki I. Skyrmion robustness in noncentrosymmetric magnets with axial symmetry: The role of anisotropy and tilted magnetic fields. *Phys. Rev. B* **96**, 214413 (2017).
47. Wan X, Hu Y, Wang B. Controlling stability and emergent rotation of the skyrmion crystal in thin films of helimagnets via tilted magnetic field. *Phys. Rev. B* **99**, 180406 (2019).
48. Bogdanov A, Hubert A. Thermodynamically stable magnetic vortex states in magnetic crystals. *JMMM* **138**, 255-269 (1994).
49. Wang L, *et al.* Ferroelectrically tunable magnetic skyrmions in ultrathin oxide heterostructures. *Nat. Mater.* **17**, 1087-1094 (2018).
50. Iwasaki J, Mochizuki M, Nagaosa N. Universal current-velocity relation of skyrmion motion in chiral magnets. *Nat. Commun.* **4**, 1463 (2013).
51. Tang C, Sellappan P, Liu Y, Xu Y, Garay JE, Shi J. Anomalous Hall hysteresis in  $\text{Tm}_3\text{Fe}_5\text{O}_{12}/\text{Pt}$  with strain-induced perpendicular magnetic anisotropy. *Phys. Rev. B* **94**, 140403 (2016).
52. Lim ZS, *et al.* Emergent Topological Hall Effect at a Charge-Transfer Interface. *Small* **16**, 2004683 (2020).

**Figures:**

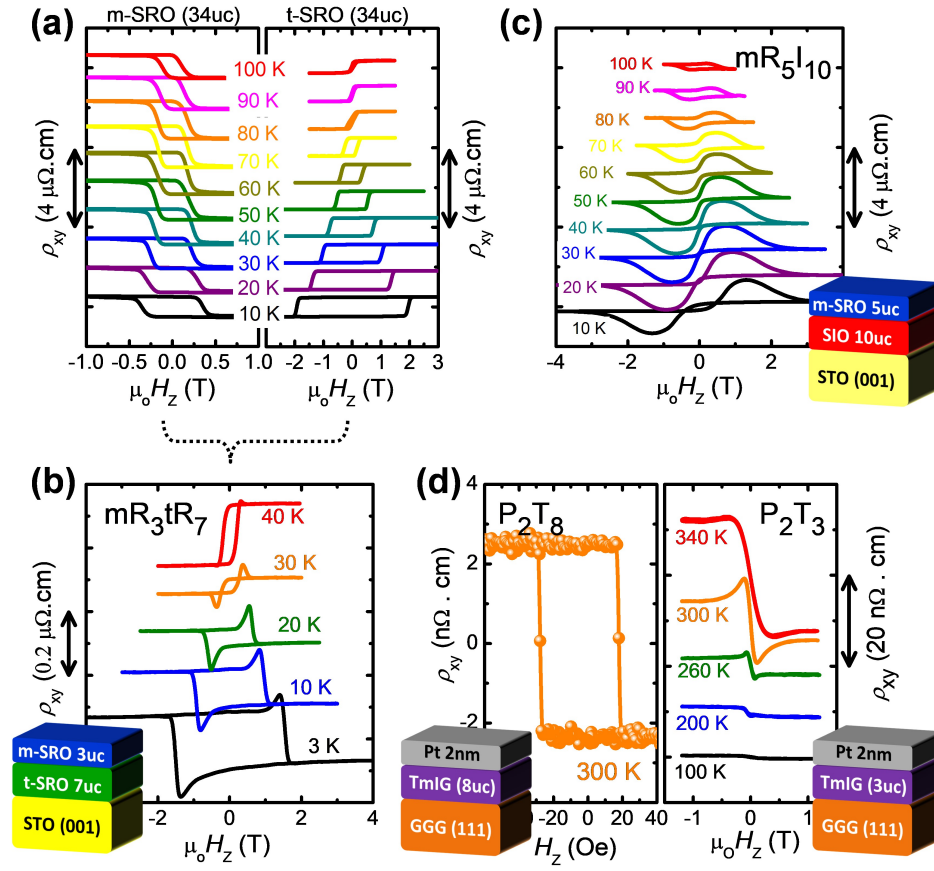


**Figure 1: Introductions of Hall Effects in various materials systems. (a)** Usual AHE loops of m- and t-phases SRO thick films on STO(001) without Hall-humps. **(b)** mR<sub>3</sub>tR<sub>7</sub> and **(c)** mR<sub>5</sub>I<sub>10</sub> on STO(001) with obvious Hall-humps. **(d)** Pt-capped TmIG films on GGG(111) substrates with 8uc (9.6nm) (left) and 3uc (3.6nm) TmIG for a consistent comparison with the SRO-based heterostructures (a-c). All linear Ordinary Hall Effect (OHE) components were removed by linear background subtraction (not shown). All data are vertically shifted for clarity.

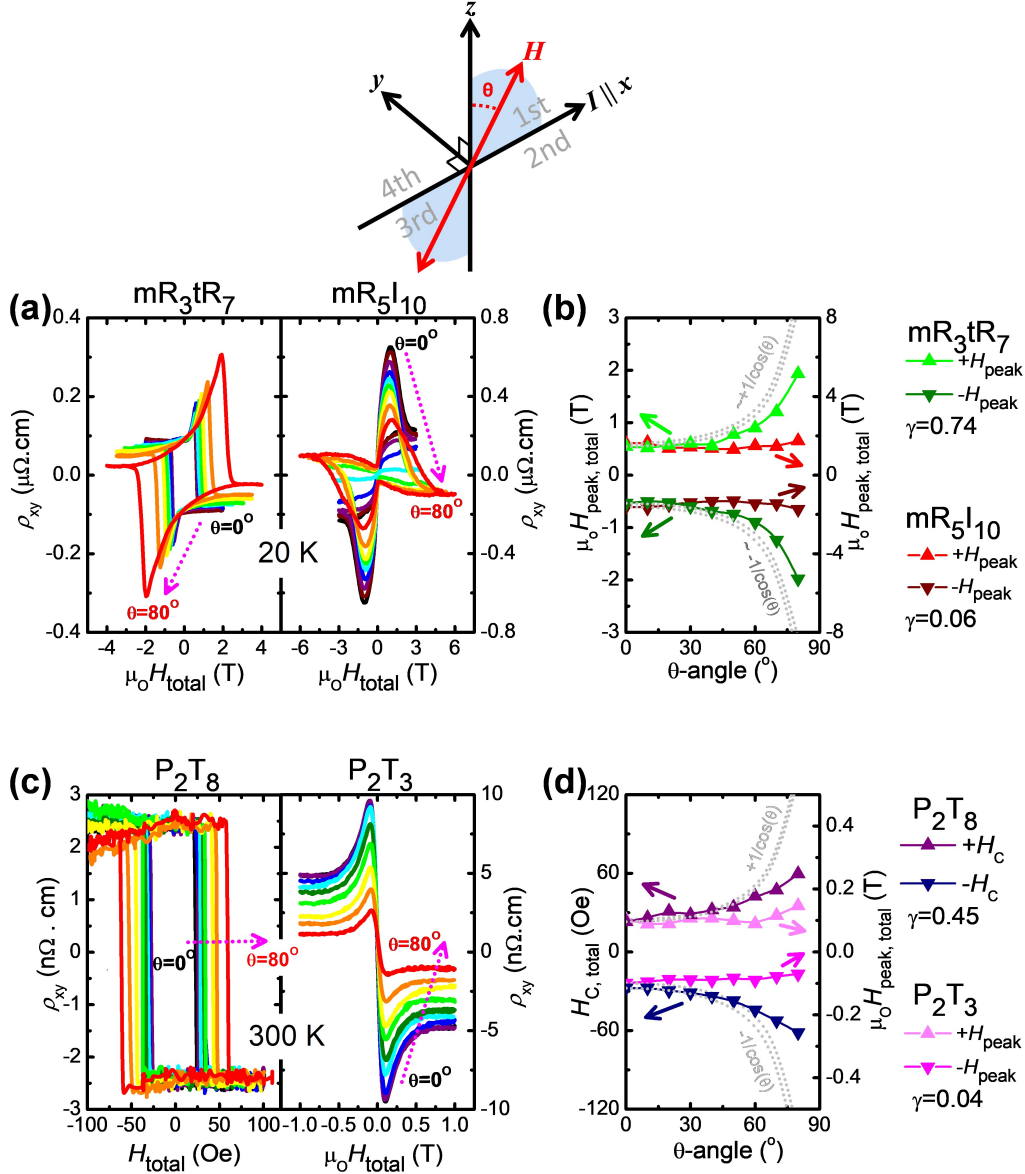


**Figure 2: Total field rotation scheme in the x-z plane.** Top: Sketch of  $\rho_{xy}(\theta, H)$  measurement configuration, where the DC current defines the x-direction and field sweep in the 1<sup>st</sup> and 3<sup>rd</sup> quadrants. (a)  $\rho_{xy}(H)$  loops of  $mR_3tR_7$  (left) and  $mR_5I_{10}$  (right) at various  $\theta$ -angles. (b) The summary of  $H_{\text{peak}}$  with  $\theta$  extracted from (a), compared to the  $1/\cos^1(\theta)$  trends (dotted lines) and the respective  $\gamma$ -values are labelled. (c)  $\rho_{xy}(H)$  loops of  $P_2T_8$  (left) and  $P_2T_3$  (right) at various  $\theta$ -angles. (d) Summary of  $H_c$  and  $H_{\text{peak}}$  extracted from (c).

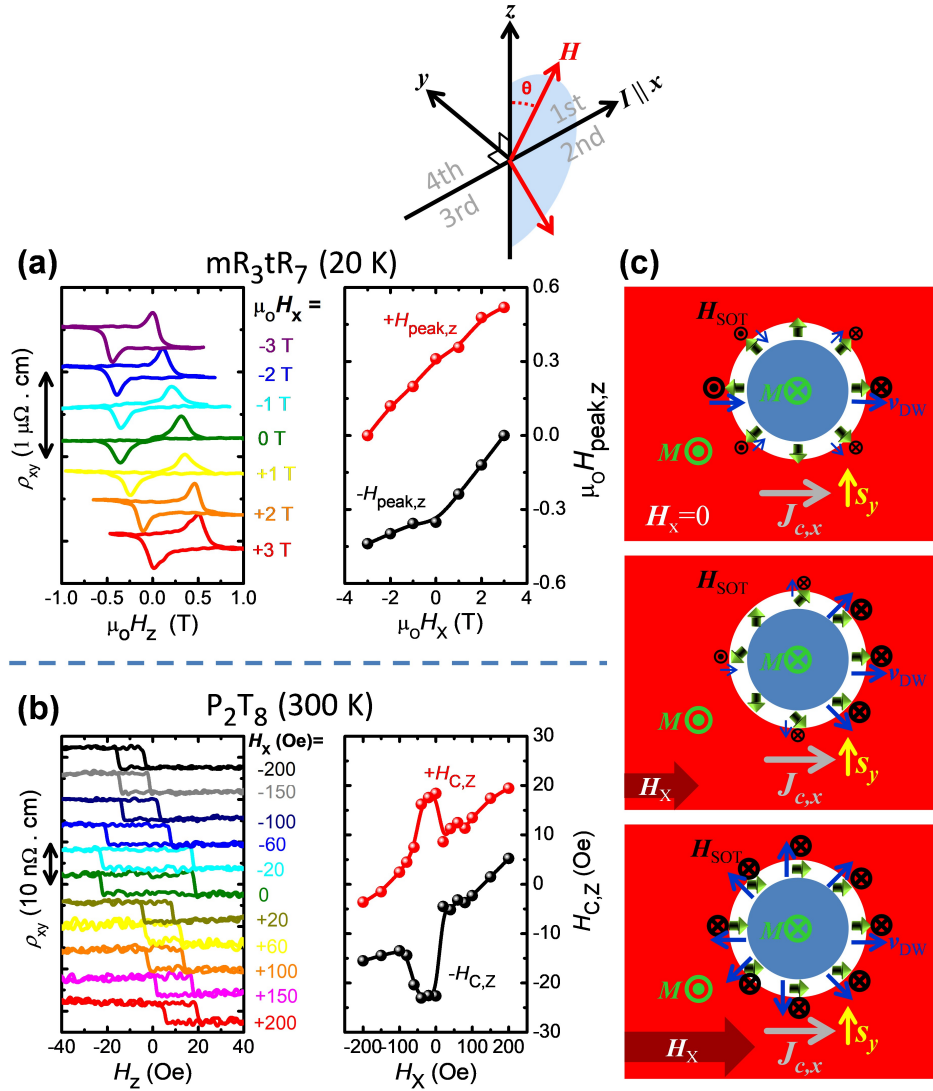


**Figure 3: Resolved field components scheme in the x-z plane.** Top: Sketch of  $\rho_{xy}(H_x, H_z)$  measurement configuration, where both the  $H_T$  and  $\theta$  are varying in the 1<sup>st</sup> and 2<sup>nd</sup> quadrants for each data point to maintain a constant  $H_x$ . **(a,b)** Left panels:  $H_x$ -dependent  $\rho_{xy}(H_z)$  loop-shifting for mR<sub>3</sub>tR<sub>7</sub> (a) and P<sub>2</sub>T<sub>8</sub> (b), where loops are vertically shifted for clarity. Right panels, summaries of z-component  $H_{\text{peak}}$  (a) and  $H_c$  (b) variations with  $H_x$ . The charge current density  $J_{c,x}$  used was  $+6.24 \times 10^8 \text{ A/m}^2$  for mR<sub>3</sub>tR<sub>7</sub> and  $+7.5 \times 10^9 \text{ A/m}^2$  for P<sub>2</sub>T<sub>8</sub>. **(c)** Effect of increasing  $H_x$  on domain wall movements. Red and blue background represents uniform magnetization pointing-up and down, while grey, yellow, brown, green, black, and blue arrows represent  $J_{c,x}$ ,  $s_y$ ,  $H_x$ ,  $m$ ,  $H_{\text{SOT}}$ ,  $v_{\text{DW}}$  vectors. The spin current  $J_{s,z}$  is not shown.

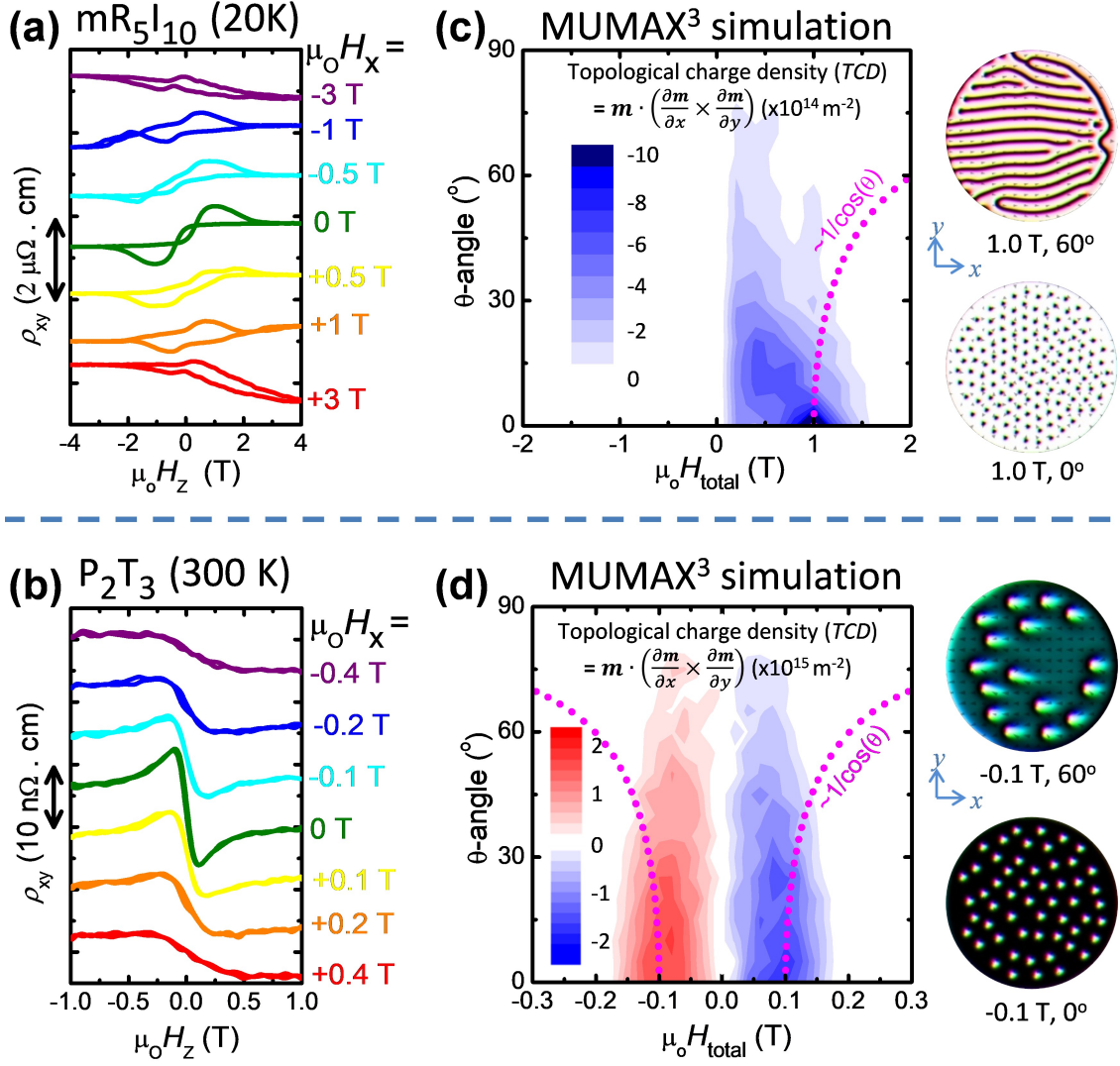


**Figure 4: Skyrmion systems investigated under the resolved field components scheme and micromagnetic simulations.** Hall-humps in mR<sub>5</sub>I<sub>10</sub> (a) and P<sub>2</sub>T<sub>3</sub> (b) vanish without shifting field-position under  $H_x$  variation.  $J_{\text{e,x}}$  used was  $+2 \times 10^8 \text{ A/m}^2$  for mR<sub>5</sub>I<sub>10</sub> and  $+2 \times 10^9 \text{ A/m}^2$  for P<sub>2</sub>T<sub>3</sub>, lower than those in Figure 3 to minimize effect of spin-orbit torque. Data are shifted vertically for clarity. (c,d) Mapping of TCD versus  $\theta$  and total field obtained by MUMAX<sup>3</sup> using realistic parameters for mR<sub>5</sub>I<sub>10</sub> and P<sub>2</sub>T<sub>3</sub> respectively. Right panels: snapshots of magnetic textures extracted from the  $(\theta, H_{\text{total}})$  states indicated by grey arrows.

Samples	$K_U$ (kJ/m <sup>3</sup> )	$A_{ex}$ (pJ/m)	$D$ (mJ/m <sup>2</sup> )	$\sigma_{DW}$ (mJ/m <sup>2</sup> )	$\gamma$
mR <sub>5</sub> I <sub>10</sub>	24.8	3.43	0.76	-1.22	0.06
mR <sub>5</sub> I <sub>10</sub> (sim.)	24.8	3.43	0.76	-1.22	-0.34
P <sub>2</sub> T <sub>3</sub>	1	5.76	0.06	-0.0925	0.04
P <sub>2</sub> T <sub>3</sub> (sim.)	1	5.76	0.06	-0.0925	-0.19
Ca-Mb <sub>3</sub> I <sub>19</sub> Mt <sub>3</sub>	6.54	1.23	0.42	-0.96	0.15
B <sub>20</sub> S <sub>5</sub>	430	2.3	0.84	1.34	0.58
B <sub>12</sub> S <sub>8</sub> (10 K)	202	3.4	0.84	0.68	0.44
(B <sub>4</sub> S <sub>4</sub> ) <sub>x4</sub> 20 K	200.2	3.4	0.84	0.67	0.63
(B <sub>4</sub> S <sub>4</sub> ) <sub>x4</sub> 40 K	70.8	3.4	0.58	0.14	0.57
mR <sub>3</sub> tR <sub>7</sub>	107.9	3.2	0.1*	2.05	0.74
P <sub>2</sub> T <sub>8</sub>	13.14	1.07	5.2x10 <sup>-3</sup>	0.46	0.45

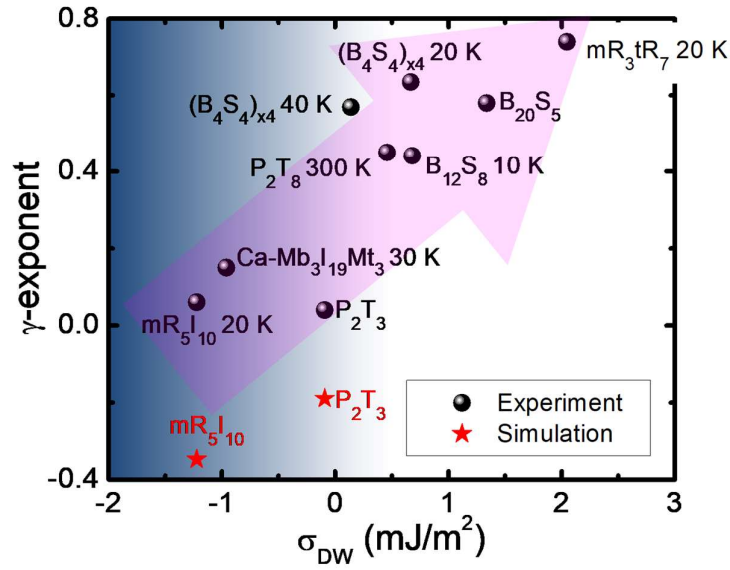


**Figure 5: Summary of  $\gamma$  versus  $\sigma_{DW}$  trend.** Top panel: table of data which generates the plot (bottom panel).  $\gamma$ -exponents plotted in black were experimentally obtained but in red for simulation (sim.). Several data were extracted from references, namely,  $K_U$  and  $D$  of P<sub>2</sub>T<sub>8</sub> from ref. [51] and [43] respectively, Ca-Mb<sub>3</sub>I<sub>19</sub>Mt<sub>3</sub> from ref. [52],  $K_U$ ,  $A_{ex}$  and  $D$  of B<sub>20</sub>S<sub>5</sub> from ref. [49], while B<sub>12</sub>S<sub>8</sub> and (B<sub>4</sub>S<sub>4</sub>)<sub>x4</sub> used the same  $D$  as B<sub>20</sub>S<sub>5</sub>. The rest of parameter values were experimentally determined in this work (refer to supplementary text).



## Supplementary Information:

### Crossover in Hump-shape Hall Effect from Karplus-Luttinger to Topological Origins

#### Elucidated by In-plane Magnetic Fields

In supplementary Fig. S1a, the half-integer XRD peaks of m-SRO and t-SRO thick films (34uc) are shown, with notations and HKL-indices following the Glazer's rules<sup>1,2</sup>. We believe that the broad humps around (0.5,1.5,1) are measurement artifacts. Considering that bulk m-SRO material is known to belong to the  $pbnm$  space group with  $a^-a^+c^+$  tilt pattern, its in-phase (+) oxygen octahedral rotation axis should have shorter B-O-B bond length. Since the STO(001) substrate imposes an in-plane compressive strain to the film, it is energetically favourable for the in-phase rotation axis of m-SRO to align with the equivalent in-plane compressive axes “ $a$ ” or “ $b$ ”<sup>3</sup>. Hence,  $a^-a^+c^+$  should not occur in thin film cases, while  $a^-b^+c^-$  and  $a^+b^-c^-$  may occur with equal probability<sup>3,4,5</sup>. In our case, strong peaks HKL=(0.5,0.5,1.5) and (1.5,0.5,1.5), supports the existence of  $a^-$ . Then, a peak at (0.5,0,1.5) supports  $b^+$  and rules out  $b^-$ , hence  $c^-$  can be deduced from (0.5, 1.5,1.5), forming  $a^-b^+c^-$ . In t-SRO(34uc), most peaks are suppressed, consistent to tetragonal  $a^0a^0c^0$  which is also partially stabilized by oxygen vacancies<sup>6</sup>. Nevertheless, a sharp peak occurs at exactly (0.5,0.5,1.5), possibly due to defects. Similarly, almost all Half-integer XRD peaks are suppressed in mR<sub>3t</sub>R<sub>7</sub> due to the dominant t-SRO and small overall thickness.

For mR<sub>5</sub>I<sub>10</sub>, the tilt/rotation patterns and their gradual transformation are illustrated in Fig. S1b (right panel), following the observation from Fig. S1a. After relaxing from suppression of tilt/rotation by the substrate, the  $a^+$  and  $b^+$  are more likely to form. Hence, the peak at (0,0.5,1.5) belongs to the  $a^+$  of the bottom SIO film (grown at 100 mTorr). In fact, the SIO film was deliberately designed to be thick enough for relaxation from strain and tilt-suppression. This way, the SIO film near the SRO/SIO interface can be assigned to  $a^+b^0c^0$ .

Subsequently, the top SRO can be expected to have weak  $a^-b^+c^0$ , bearing much resemblance to the thick m-SRO (34uc) with  $a^-b^+c^-$ . Previously in reference <sup>7</sup>, we have discussed that the thick enough bottom SIO with relaxation from  $a^0b^0c^0$  to  $a^+b^0c^0$  is crucial to achieve the Hall-humps. Replacing the bottom SIO with a low pressure grown one with the same thickness will again result in total suppression in almost all half-interger XRD peaks as well as a defect peak occurring at (0.5,0.5,1.5), since oxygen vacancies in SIO also tend to stabilize tetragonal crystal structure, leading to suppression of Hall-humps.

### First-principle Calculations

In Density Functional Theory (DFT) calculations for Dzyaloshinskii-Moriya Interaction (DMI), we limit the structure in each case to a two-unit cell thin slab for optimal computational cost. Hence, the initial structure of mR<sub>3</sub>tR<sub>7</sub> follows the bracketed interfacial region in Fig. S1b which shows a transition from the bottom t-SRO ( $a^0a^0c^0$ ) to top m-SRO ( $a^-b^+c^-$ ). The lattice parameters  $a$  and  $b$  are fixed at 3.9053 Å following the substrate, and  $c = 4.04$  Å and 3.94 Å for the unit cells below and above the interface respectively. Likewise the initial structures of mR<sub>5</sub>I<sub>10</sub> is an interfacial slab of SIO ( $a^+b^0c^0$ ) below SRO ( $a^-b^+c^0$ ) bracketed in Fig. S1c, with lattice parameters  $a=b=3.9053$  Å, whereas  $c = 3.95$  Å (bottom) and 3.94 Å (top).

Next, the Vienna *Ab-initio* Simulation Package (VASP) package was employed in three steps <sup>8</sup>. Firstly, structural relaxations were performed on top of the input obtained from half-integer HKL XRD until the forces become smaller than 0.01 eV/Å for determining the moststable interfacial geometries, resulting in small adjustments from the input. Secondly, the Kohn-Sham equations were solved, with no SOC, to find out the charge distribution of the system's ground state. Finally, SOC was included and the self-consistent total energies of the system were determined as a function of the Ru<sup>4+</sup> magnetic moment orientations (cycloidal wavevector  $q$ ) which were controlled by using the constrained method implemented in VASP.

## Magnetometry and MUMAX<sup>3</sup> Micromagnetic Simulations

In Fig. S4, the magnetometry data of mR<sub>3</sub>tR<sub>7</sub>, mR<sub>5</sub>I<sub>10</sub>, B<sub>12</sub>S<sub>8</sub>, (B<sub>4</sub>S<sub>4</sub>)<sub>x4</sub>-SL are shown. The  $M$ - $H$  loops with  $\mathbf{H}||c$  (out-of-plane) and  $\mathbf{H}||a$  (in-plane) at the left panels are useful to calculate magnetic anisotropy and inference of saturation magnetization ( $M_{\text{sat}}$ ) at various temperatures. The Curie temperatures ( $T_C$ ) can be inferred from the moment versus temperature ( $M$ - $T$ ) from the right panels. The field-cooling (FC)  $M$ - $T$  curves of Figure S4b extending to higher temperature cut-offs (~150 K) than the zero-field-cooled (ZFC)  $M$ - $T$  curves are likely due to the proximity-induced magnetism and spin-liquid behaviour of SIO film. These information are used as MUMAX<sup>3</sup> simulation, using the following equations:

$$A_{\text{ex}} = \frac{3k_B T_C}{2j(j+1)a} \quad ; \quad l_{\text{ex}} = \sqrt{\frac{2A_{\text{ex}}}{\mu_0 M_{\text{sat}}^2}} \quad ; \quad K_u = \int_0^{H_{\text{sat}}} (M_{H||c} - M_{H||a}) \cdot dH$$

where  $A_{\text{ex}}$ ,  $j$ ,  $a$ ,  $l_{\text{ex}}$  and  $K_u$  are the exchange stiffness, total angular momentum quantum number per formula unit, lattice parameter, exchange length and uniaxial magnetic anisotropy respectively. Since Ru<sup>4+</sup> (4d<sup>4</sup>) is lying between the weak SOC (l-s coupling) and strong SOC (j-j coupling) regimes with spin and orbital angular momentum of S=1, L=1, the SRO has j=1 because the two vectors are neither parallel nor antiparallel. While j=5/2 is typically suitable for Fe<sup>3+</sup> (3d<sup>5</sup>) with S=5/2 and L=0 in TmIG.

For SRO-based heterostructures, relatively low temperatures are chosen for  $K_u$  calculations as indicated in the  $M$ - $H$  curves (Fig. S4) to match the fact that the DMI values extracted from DFT are ground state (0 K) values, and we do not know how DMI reduces with thermal fluctuation. This strategy facilities a good trend in main text Figure 5. Due to difficulty in measuring precise magnetometry data for TmIG thin films grown on highly-paramagnetic GGG(111) substrates,  $K_u$  of P<sub>2</sub>T<sub>8</sub> were extracted from reference [9] showing anisotropy field,  $H_K = 1460$  Oe, and  $K_u \approx \mu_0 M_{\text{sat}} H_K = 13140 \text{ J/m}^3$  while  $M_{\text{sat}} = 90 \text{ emu/cm}^3 = 9 \times 10^4 \text{ A/m}$ . Whereas  $T_C$  of P<sub>2</sub>T<sub>8</sub> and P<sub>2</sub>T<sub>3</sub> can be confidently estimated to be 550 K and 300 K

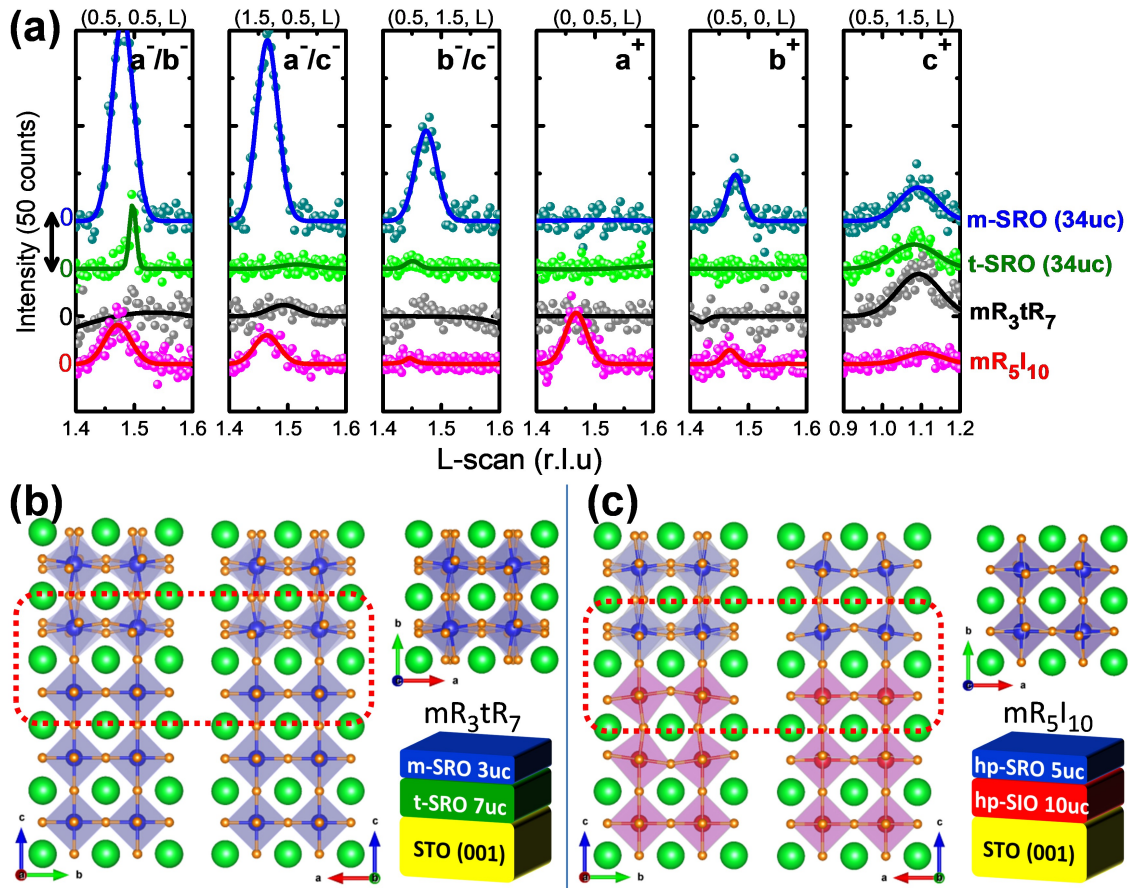
respectively, since 550 K is known to be the bulk value of garnet ferrites<sup>10</sup>, while from the main text Figure 1d (right panel) of this manuscript we can see a divergence of Hall-hump (THE) in  $P_2T_3$  around 300 K, consistent to the power-law scaling of  $\rho_{xy}^T \propto |T - T_C|^{-\gamma'}$  discussed in reference [11]. A simulation grid cell size of  $4 \text{ nm} < l_{\text{ex}}$  was used for all cases, with  $256 \times 256$  meshes in the xy-plane but 1-cell in the z-direction thickness. The backward/forward field sweep simulations are always initialized with  $m = \text{Uniform}(0, 0, \pm 1)$  to retain the history of magnetization saturation. Each simulation was terminated after reaching a criterion of max-torque  $< 5 \times 10^{-3}$ . The simulation parameters for  $mR_5I_{10}$  and  $P_2T_3$  are shown in the table below, resulting in hysteretic  $TCD$  in  $mR_5I_{10}$  but non-hysteretic  $TCD$  in  $P_2T_3$ .

	$T_C$	$j$	$a$	$A_{\text{ex}}$	$M_{\text{sat}}$	$K_U$	$D_{\text{ind}}$	$l_{\text{ex}}$	Thickness	$a_G$
Unit	K		$\text{\AA}$	pJ/m	kA/m	kJ/m <sup>3</sup>	mJ/m <sup>2</sup>	nm	nm	
$mR_5I_{10}$	125	1	3.93	3.43	63	25	0.76	36.3	1.97	0.1
$P_2T_3$	300	5/2	12.3	0.58	20	10	0.1	47.9	3.70	0.03

## References:

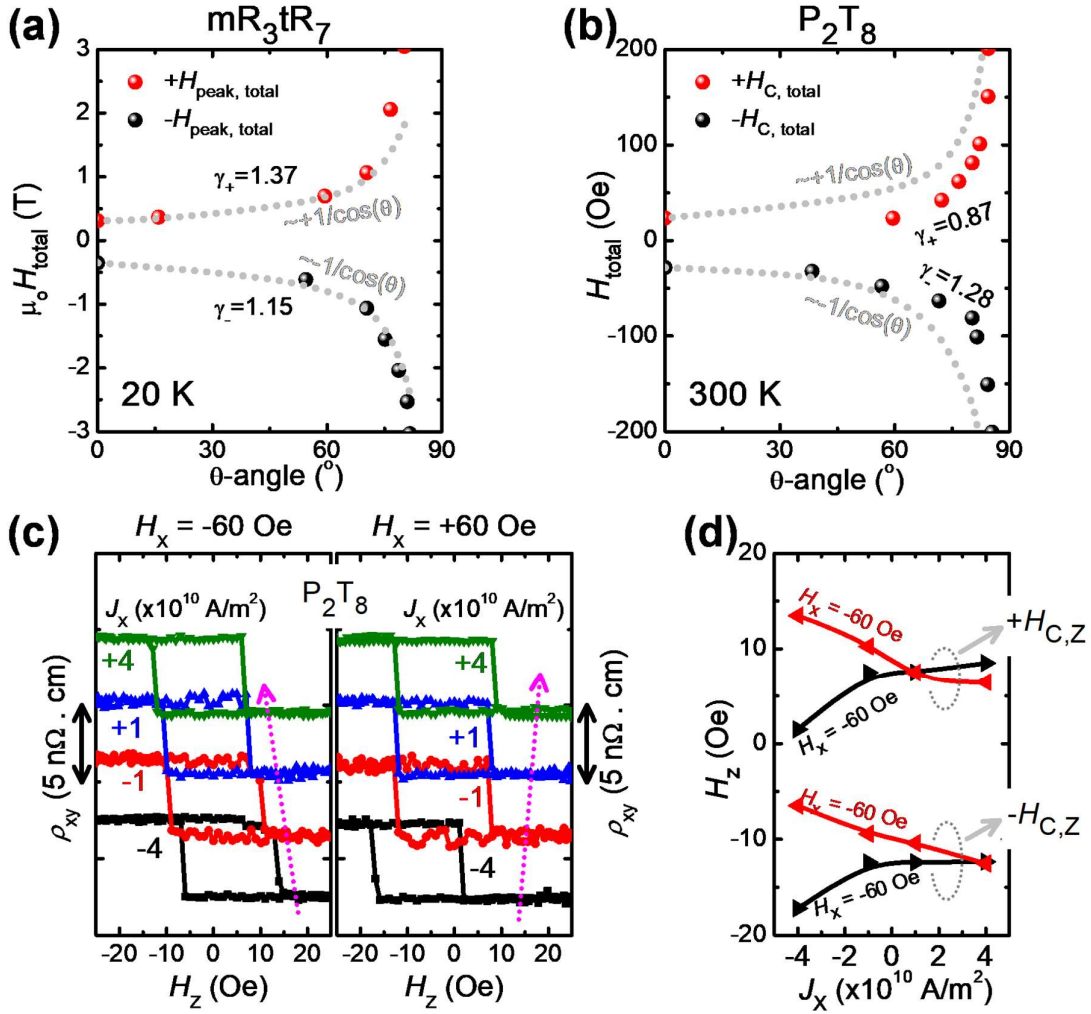
1. Glazer AM. The classification of tilted octahedra in perovskites. *AcCrB* **28**, 3384-3392 (1972).
2. Glazer AM. Simple ways of determining perovskite structures. *AcCrA* **31**, 756-762 (1975).
3. van Thiel TC, *et al.* Coupling Lattice Instabilities Across the Interface in Ultrathin Oxide Heterostructures. *ACS Materials Letters* **2**, 389-394 (2020).
4. Nie YF, *et al.* Interplay of Spin-Orbit Interactions, Dimensionality, and Octahedral Rotations in Semimetallic SrIrO<sub>3</sub>. *Phys. Rev. Lett.* **114**, 016401 (2015).
5. Schütz P, *et al.* Dimensionality-Driven Metal-Insulator Transition in Spin-Orbit-Coupled SrIrO<sub>3</sub>. *Phys. Rev. Lett.* **119**, 256404 (2017).
6. Lu W, Yang P, Song WD, Chow GM, Chen JS. Control of oxygen octahedral rotations and physical properties in SrRuO<sub>3</sub> films. *Phys. Rev. B* **88**, 214115 (2013).
7. Zhi Shih Lim AKHK, Zhou Zhou, Ganesh Ji Omar, Ping Yang, Robert Laskowski, Ariando Ariando. Oxygen Octahedral Tilt Controlled Topological Hall Effect in Epitaxial and Freestanding SrRuO<sub>3</sub>/SrIrO<sub>3</sub> Heterostructures. *arXiv.org*, (2022).
8. Yang H, Thiaville A, Rohart S, Fert A, Chshiev M. Anatomy of Dzyaloshinskii-Moriya Interaction at Co/Pt Interfaces. *Phys. Rev. Lett.* **115**, 267210 (2015).
9. Tang C, Sellappan P, Liu Y, Xu Y, Garay JE, Shi J. Anomalous Hall hysteresis in Tm<sub>3</sub>Fe<sub>5</sub>O<sub>12</sub>/Pt with strain-induced perpendicular magnetic anisotropy. *Phys. Rev. B* **94**, 140403 (2016).
10. Pauthenet R. Spontaneous Magnetization of Some Garnet Ferrites and the Aluminum Substituted Garnet Ferrites. **29**, 253-255 (1958).
11. Raju M, *et al.* Colossal topological Hall effect at the transition between isolated and lattice-phase interfacial skyrmions. *Nat. Commun.* **12**, 2758 (2021).

**Supplementary Figures:**



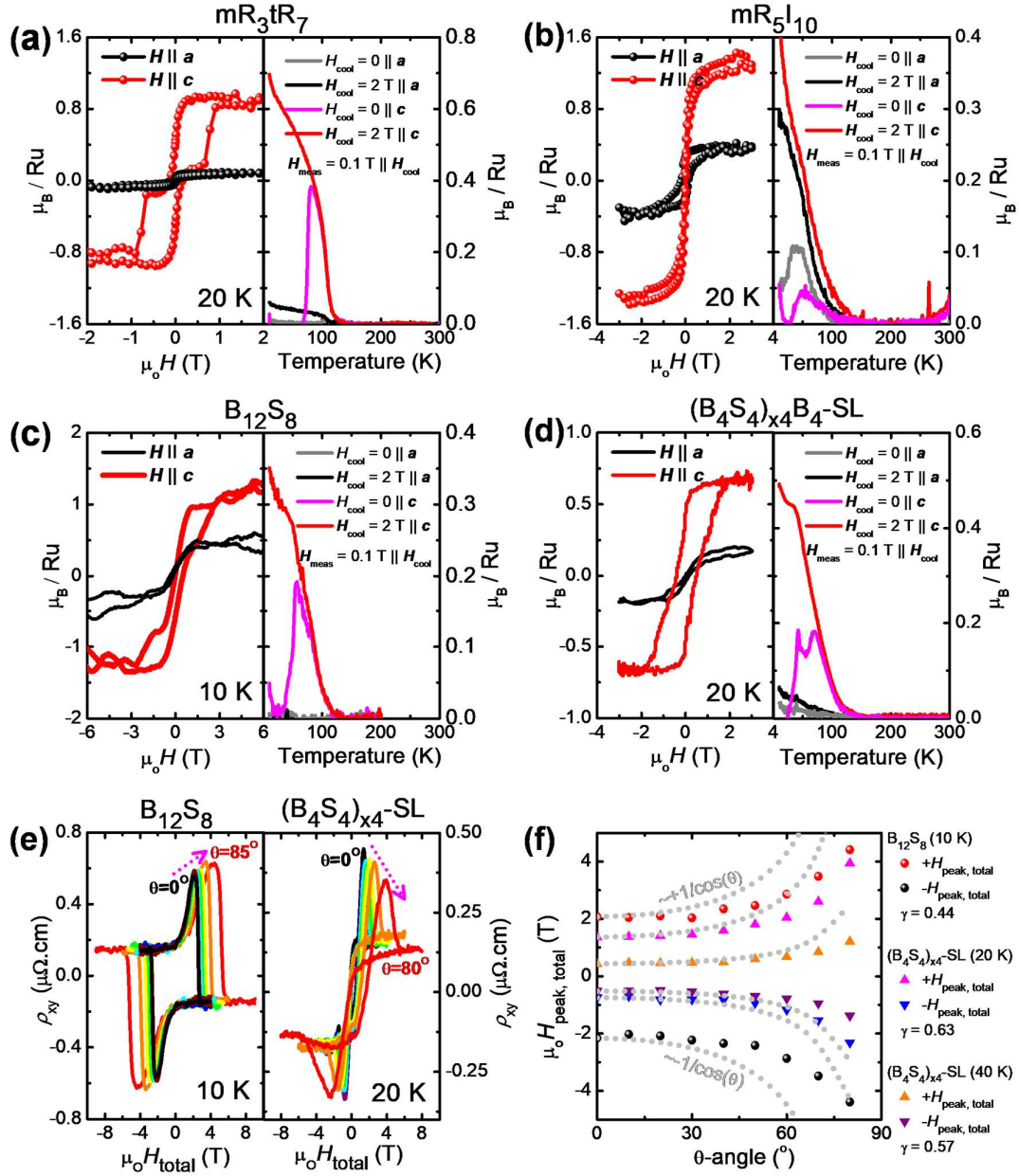
**Supplementary Figure S1:** (a) Half-integer X-ray Bragg diffraction data for thick films of m-SRO and t-SRO, mR<sub>3</sub>tR<sub>7</sub> and mR<sub>5</sub>I<sub>10</sub>. Structural models for DFT calculations of DMI for (b) mR<sub>3</sub>tR<sub>7</sub> and (c) mR<sub>5</sub>I<sub>10</sub> as deduced from (a). The left, middle and right panels are views from  $a$ ,  $b$ , and  $c$ -axes. The red dotted lines in (b) and (c) demarcate the actual regions used in DFT calculations.

**Supplementary Figure S2:** DFT calculation results for **(a)** mR<sub>3t</sub>R<sub>7</sub> and **(b)** mR<sub>5I</sub>I<sub>10</sub>. The DMI value obtained are 0.76 and 0.76 mJ/m<sup>2</sup> respectively.



**Supplementary Figure S3:** The resulted  $\theta$ -angle dependent  $H_{\text{peak, total}}$  or  $H_{\text{C, total}}$  trends after transforming the  $H_{\text{peak, z}}$  and  $H_{\text{C, z}}$  data from the resolved field-component scheme in main text Figure 3 for **(a)** mR<sub>3</sub>tR<sub>7</sub> and **(b)** P<sub>2</sub>T<sub>8</sub>. The  $\gamma$ -exponents for the positive and negative branches are labelled. The meaning of  $\gamma > 1$  is currently not well-understood. In P<sub>2</sub>T<sub>8</sub>, no sign of reduction/shrinkage can be seen in  $H_{\text{C, total}}$  with increasing  $\theta$ , although reduction in  $H_{\text{C, z}}$  with increasing  $H_x$  is observed at small  $H_x$ . **(c)**  $\rho_{xy}$  versus  $H_z$  Hall-loops at constant  $H_x = \pm 60$  Oe but with varying  $J_x$  from  $-4 \times 10^{10}$  to  $+4 \times 10^{10}$  A/m<sup>2</sup> showing clear shifts, with the z-component coercive fields ( $H_{\text{c, z}}$ ) plotted in **(d)**. The shifting direction reverses upon reversing the sign of  $H_x$  is a clear signature of SOT effect.





**Supplementary Figure S4:** Magnetometry data for (a) mR<sub>3tR7</sub> (b) mR<sub>5I10</sub> (c) B<sub>12</sub>S<sub>8</sub> and (d) (B<sub>4</sub>S<sub>4</sub>)<sub>x4</sub>-SL respectively. In each heterostructure, the  $M-H$  curves for in-plane and out-of-plane fields are plotted on the left panels for calculations of  $K_U$  at the temperature indicated, while  $M-T$  are plotted on the right panels for calculation of  $A_{ex}$  from extracted  $T_C$ . (e) Hall-loops with increasing  $\theta$ -angle in the total-field rotation scheme for B<sub>12</sub>S<sub>8</sub> at 10 K (left) and (B<sub>4</sub>S<sub>4</sub>)<sub>x4</sub>-SL at 20 K (right). (f) The divergence trend of  $H_{peak, total}$  with increasing  $\theta$  including (B<sub>4</sub>S<sub>4</sub>)<sub>x4</sub>-SL at 40 K, with the  $\gamma$ -exponent for each case labelled at the legend.